

HIGH-RESOLUTION X-RAY SPECTROSCOPY OF THE INTERSTELLAR MEDIUM II: NEON AND IRON ABSORPTION EDGES

ADRIENNE M. JUETT¹, NORBERT S. SCHULZ², DEEPTO CHAKRABARTY^{2,3} AND THOMAS W. GORCZYCA⁴*Accepted for Publication in the Astrophysical Journal*

ABSTRACT

We present high-resolution spectroscopy of the neon K -shell and iron L -shell interstellar absorption edges in nine X-ray binaries using the High Energy Transmission Grating Spectrometer (HETGS) onboard the *Chandra X-ray Observatory*. We found that the iron absorption is well fit by an experimental determination of the cross-section for metallic iron, although with a slight wavelength shift of ≈ 20 mÅ. The neon edge region is best fit by a model that includes the neutral neon edge and three Gaussian absorption lines. We identify these lines as due to the $1s-2p$ transitions from Ne II, Ne III, and Ne IX. As we found in our oxygen edge study, the theoretical predictions for neutral and low-ionization lines all require shifts of ≈ 20 mÅ to match our data. Combined with our earlier oxygen edge study, we find that a best fit O/Ne ratio of 5.4 ± 1.6 , consistent with standard interstellar abundances. Our best fit Fe/Ne ratio of 0.20 ± 0.03 is significantly lower than the interstellar value. We attribute this difference to iron depletion into dust grains in the interstellar medium. We make the first measurement of the neon ionization fraction in the ISM. We find $\text{Ne II/Ne I} \approx 0.3$ and $\text{Ne III/Ne I} \approx 0.07$. These values are larger than is expected given the measured ionization of interstellar helium. For Ne IX, our results confirm the detection of the hot ionized interstellar medium of the Galaxy.

Subject headings: ISM: general — X-rays: ISM — X-rays: binaries

1. INTRODUCTION

High-resolution X-ray spectral observations from the *Chandra X-ray Observatory* and *XMM-Newton* offer a new tool with which to study the interstellar medium (ISM). The ISM affects X-ray spectra in two ways: photoelectric absorption, particularly at low energies (0.1–10 keV), and scattering by dust grains, producing X-ray halos. At X-ray energies, absorption features are primarily from the excitation and ionization of inner-shell (K -shell) electrons, although for high- Z elements like iron, L -shell absorption edges are also detectable. Measurements of the ISM absorption features in the spectra of X-ray binaries allow us to study the abundances and ionization fractions for a large number of elements, analogous to optical and ultraviolet observations of stars that measure ISM absorption features. Additionally, high-resolution X-ray spectral measurements provide a new method for determining the elemental depletion of the ISM and composition of interstellar dust.

The first attempt to measure ISM absorption edges in the X-rays used the *Einstein* Focal Plane Crystal Spectrometer (Schattenburg & Canizares 1986) and found evidence for the O I $1s-2p$ ($K\alpha$) absorption resonance and a possible O II edge. Recent *Chandra* and *XMM* results have revealed more complex structure around the oxygen K -shell absorption edge (Paerels et al. 2001; Schulz et al. 2002; Takei et al. 2002; de Vries et al. 2003; Juett et al. 2004, hereafter Paper I). All of the high-resolution work points to a complex system of absorp-

tion features at or near the oxygen edge, which is not the simple step function used in absorption models. Similar high-resolution structure is expected at all of the absorption edges.

Previous results from *Einstein* and *EXOSAT* grating observations of the bright low mass X-ray binary (LMXB) Sco X-1 point to an underabundance of oxygen and an overabundance of nitrogen along the line of sight to the source (Kahn et al. 1984; Brinkman et al. 1985). Similarly, using the abundances of Anders & Grevesse (1989, O/H = 8.51×10^{-4}), Weisskopf et al. (2004) found that the spectrum of the Crab pulsar was best-fit when oxygen was underabundant. When the newer abundances of Wilms et al. (2000, O/H = 4.90×10^{-4}) were used, oxygen was not required to be underabundant, although a slightly lower than nominal oxygen abundance was preferred, O/H = $(3.33 \pm 0.25) \times 10^{-4}$. We note that the measurement of the oxygen abundance relative to hydrogen is misleading since the X-ray band can not directly measure the hydrogen column density. Instead, the measurement is relative to the absorption from other metals which are converted to an equivalent hydrogen column density using standard abundances. Takei et al. (2002) compared the oxygen and neon column densities measured in the X-ray to the hydrogen column density from radio observations along the line of sight to Cyg X-2. Both the neon and oxygen abundances were found to be $\approx 3/4$ the solar abundances of Anders & Grevesse (1989) but in line with newer estimates of ISM abundances (e.g., Wilms et al. 2000). Finally, Ueda et al. (2005) found an overabundance relative to oxygen for magnesium, silicon, sulfur, and possibly iron (assuming solar abundance ratios from Anders & Grevesse 1989) in the ISM absorption along the line of sight to three bright neutron star LMXBs. While many X-ray binaries have absorption which is well described by standard abundances, some systems have shown unusual abundance ra-

¹ Department of Astronomy, University of Virginia, Charlottesville, VA 22903; ajuett@virginia.edu

² Kavli Institute for Astrophysics and Space Research, Massachusetts Institute of Technology, Cambridge, MA 02139

³ Department of Physics, Massachusetts Institute of Technology, Cambridge, MA 02139

⁴ Department of Physics, Western Michigan University, Kalamazoo, MI 49008

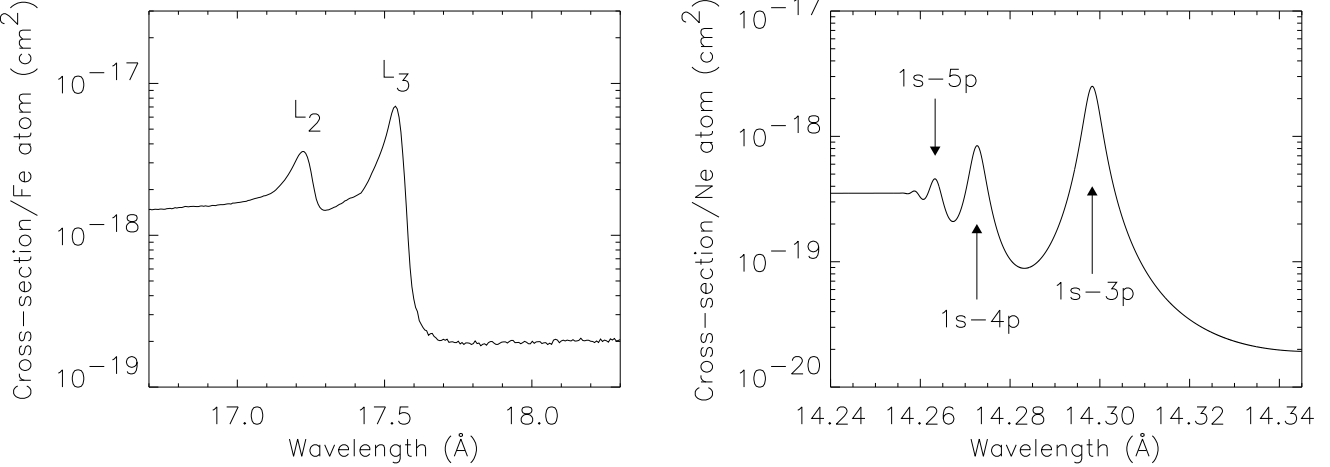


FIG. 1.— *Left panel*: Iron L -shell cross-section as a function of wavelength for metallic iron (Kortright & Kim 2000). The positions of the L_2 and L_3 edges are marked. *Right panel*: Neon K -shell cross-section as a function of wavelength (Gorczyca 2000). The positions of the $1s-3p$, $1s-4p$, and $1s-5p$ transitions are marked. Only the $1s-3p$ transition is resolved by *Chandra*.

tios which have been attributed to material local to these systems (Paerels et al. 2001; Juett et al. 2001; Lee et al. 2002; Juett & Chakrabarty 2003). Therefore, an accurate measurement of the relative abundances along many lines of sight is necessary in order to interpret data for sources which show unusual abundance ratios.

We also mention a new result that found a significantly larger Ne/O ratio than in standard solar or ISM models. Using the X-ray emission lines from nearby solar-like stars, Drake & Testa (2005) found an average Ne/O ratio of 0.41, or 2.7 times greater than the standard ISM or solar abundances. If the Sun has a similar Ne/O ratio then this would solve the solar helioseismology problem (see Bahcall et al. 2005). We note that this work has sparked some controversy and claims of smaller Ne/O ratios in the Sun were quickly made (Schmelz et al. 2005; Asplund et al. 2005a). In either case, it is not readily apparent that solar coronal measurements should equal the ISM abundances.

It was recognized early in the history of X-ray spectroscopy that the composition of dust grains could be probed by spectroscopic measurements of absorption edges (Martin 1970). Absorption edges from molecules include X-ray absorption fine structure (XAFS) due to the influence of nearby atoms on the absorption process (Woo 1995). Such features would distinguish between the molecular and atomic contributions to the edge structure. In addition, the resonance structure of the absorption edges is expected to be shifted, relative to the atomic position, in molecular absorption edges due to the molecular binding energy. The edges from magnesium, silicon, and iron are expected to be dominated by contributions from molecular, as opposed to atomic, forms given the high levels of depletion measured ($X_{\text{dust}}/X_{\text{total}} \gtrsim 95\%$), while carbon, oxygen, and nitrogen are only mildly depleted ($X_{\text{dust}}/X_{\text{total}} \lesssim 60\%$; Savage & Sembach 1996). Several authors have claimed detection of the $1s-2p$ transition in iron oxides (Paerels et al. 2001; Schulz et al. 2002; Takei et al. 2002), although we showed that this resonance coincides with the $1s-2p$ transition from O II

making the identification of iron oxides debatable (Paper I). Lee et al. (2002) claimed a tentative detection of XAFS in the silicon absorption edge of the X-ray binary GRS 1915+105. Similarly Ueda et al. (2005) claimed that the silicon and magnesium edges in the spectra of three LMXBs show XAFS consistent with the expected structure from silicates. In addition, depletion of elements in grains can reduce the effective cross-section for absorption due to screening (see e.g., Wilms et al. 2000). This effect will lead to deviations in the measured abundances from the true interstellar values.

Along with neutral and molecular absorption edges, features from ionized species are also expected. We showed that low ionization lines from oxygen are found in the spectra of a number of X-ray binaries (Paper I). From these lines, a measurement of the large-scale ionization fraction of oxygen in the ISM is made. Miller et al. (2004a) identified Ne II and Ne III absorption lines in the spectra of two black-hole X-ray binaries. They attributed these to material local to the systems, although such lines may arise in the ISM similar to the oxygen lines. Highly ionized lines may also be expected from the hot ionized phase of the ISM. Futamoto et al. (2004) claim the detection of an O VII absorption line in the spectrum of the LMXB 4U 1820–30, which they attribute to the hot ISM. Recently, Yao & Wang (2005) detected Ne IX absorption in the spectra of a number of LMXBs. Low-ionization lines can be used to better understand the relationship between the warm ionized and warm neutral phases of the ISM. The high-ionization features in Galactic LMXBs probe the hot ionized phase of the ISM and have direct implications for the detection of $z = 0$ highly ionized oxygen and neon absorption features in the spectra of quasars, which have been claimed to be due to the local group warm-hot intergalactic medium (e.g., Nicastro et al. 2003) or alternatively a hot Galactic corona (Sembach et al. 2003).

In this paper, we study the absorption edges of neon (K -shell) and iron (L -shell) in nine bright X-ray binaries. These edges are most prominent in systems with Galactic

hydrogen column densities of 10^{21} – 10^{22} cm $^{-2}$. Many of the X-ray binaries used in this work were also part of the oxygen edge study, allowing us to measure the relative abundances of oxygen, iron, and neon. These elements also sample a variety of expected depletion levels: neon should have no depletion, oxygen is mildly depleted, and iron is heavily depleted. We will look for signatures of depletion by comparing the abundance ratios of the elements. Finally, we will measure the ionization of neon, using the identified low- and high-ionization absorption features.

2. EXPECTED STRUCTURE OF THE IRON AND NEON ABSORPTION EDGES

In Paper I, we presented an overview of the basic atomic physics necessary to understand K -shell absorption in the X-ray band. We defer the reader to the discussion presented there and focus in the following specifically on the iron L -shell and neon K -shell absorption edges.

The iron edge located at 17.5 Å is due to the excitation and ionization of L -shell ($n = 2$) electrons. The high-resolution structure of the edge is resolved into three distinct edges, L_1 , L_2 , and L_3 . The L_1 edge at 14.7 Å, due to transitions from the $2s$ level, is the weakest of the edges and we neglect it in our study since our data are not sensitive enough to measure this absorption. The L_2 and L_3 edges, due to transitions from the $2p_{1/2}$ and $2p_{3/2}$ levels, are located at 17.2 and 17.5 Å, respectively (see Table 1 and Figure 1).

To model the cross-section from Fe- L , we use the measurement of metallic iron by Kortright & Kim (2000). A comparison of the Kortright & Kim (2000) cross-section with lower-resolution determinations (Henke et al. 1993; Verner et al. 1993; Chantler 1995) finds that the values compare to within 15% at a wavelength of 16.8 Å, where the high-resolution structure is no longer a factor. Other analyses have found that the Kortright & Kim (2000) measurement reproduces the high-resolution structure of the iron edge quite well (e.g., Lee et al. 2001; Schulz et al. 2002).

We expect the cross-section from iron in dust to differ in two important aspects. First, the shape and position of the edge can differ depending on the binding of iron within a molecule. The two most common forms of iron in molecules are ferrous (Fe^{2+}) and ferric (Fe^{3+}). Spectroscopic studies of the Fe- L edge reveal that the position of the L_3 edge varies from 17.517 Å for ferrous iron to 17.475 Å for ferric iron (van Aken & Liebscher 2002). Molecules with a mix of the two forms show a double-peaked profile. The L_2 edge position and structure also varies (van Aken & Liebscher 2002). Olivines, a favored form of interstellar dust (see e.g., Draine 2003), contains pure ferrous iron. Iron oxides can contain ferrous (FeO), ferric (Fe_2O_3), or ferrous ferric iron (Fe_3O_4), depending on the composition. Therefore, determination of the position and shape of the L_3 edge can yield information on the composition of interstellar dust.

The second difference is the strength of the cross-section for absorption. In grains, the optical depth can be large (~ 1), therefore absorption will occur primarily on the surface. Atoms located in the inner regions of the grains are shielded by the outer layers. This pro-

TABLE 1. IRON AND NEON EDGE AND LINE POSITIONS

Feature	Predicted λ (Å)	Measured ^a λ (Å)
Kortright & Kim 2000		
Fe- L_3 edge ^b	17.537	17.498 ± 0.003
Fe- L_2 edge ^b	17.226	17.188 ± 0.003
van Aken & Liebscher 2002		
Fe $^{2+}$ - L_3 edge ^b	17.517	17.498 ± 0.003
Fe $^{2+}$ - L_2 edge ^b	17.206	17.188 ± 0.003
Fe $^{3+}$ - L_3 edge ^b	17.475	17.498 ± 0.003
Fe $^{3+}$ - L_2 edge ^b	17.156	17.188 ± 0.003
Gorczyca 2000		
Ne I 1s-3p ^c	14.298	14.295 ± 0.003
Ne I 1s-4p	14.273	
Ne I 1s-5p	14.263	
Gorczyca & McLaughlin 2005		
Ne II 1s-2p	14.605	14.608 ± 0.002
Ne III 1s-2p	14.518	14.508 ± 0.002
Behar & Netzer 2002		
Ne II 1s-2p	14.631	14.608 ± 0.002
Ne III 1s-2p	14.526	14.508 ± 0.002
Ne IX 1s-2p	13.448	13.4439 ± 0.0013

^aMeasured in this work.

^bPosition measured at wavelength of maximum absorption.

^cPosition of 1s-3p transition will be coincident with edge wavelength when using a standard edge model.

duces a net reduction in the cross-section for elements located in dust grains. We have estimated this effect for iron, following the description in Wilms et al. (2000), and find that the cross-section for absorption of iron in dust grains is 88% of the cross-section for gaseous iron. We note that this calculation requires a number of assumptions, including the relative abundances and depletions of the interstellar elements (see Appendix A). A more detailed study of these assumptions is presented in Section 4.1.

The neon K -shell ($n = 1$) absorption edge is located at 14.3 Å (Gorczyca 2000). The neon edge, like oxygen, is composed of a series of resonance lines ending at the series limit or ionization energy. Neon, and higher Z elements, do not have a 1s-2p transition due to a closed 2p shell in the neutral atomic ground state configuration. Gorczyca (2000) calculated the cross-section for neutral neon absorption and found that his results closely matched experimental determinations of the cross-section (see Figure 1). The resolution of *Chandra* and *XMM* is near the limit needed to resolve the 1s-3p resonance line from the rest of the edge structure of neon, therefore we expect that when using standard edge models the measured edge positions will be consistent with the position of the 1s-3p resonance (see Table 1).

We also expect ionized neon to be present in the ISM. The primary transition we will find is from the 1s-2p transition in ionized neon. Unlike neutral neon, the 1s-2p transition is available for ionized forms. Behar & Netzer (2002) calculated the wavelengths and oscillator strengths of the strongest 1s- np (primarily 1s-2p) transitions for a variety of elements and ionizations. The authors estimate that the errors on the calculated values are $\lesssim 0.2\%$ for wavelengths and $\lesssim 10\%$ for oscillator strengths and autoionization rates. They also note

TABLE 2. OBSERVATION LOG

Source Name	ObsID	Observation Date	Time (ks)	<i>l</i>	<i>b</i>	Dist. (kpc)	$ z $ (pc)	N_{O} (10^{18} cm^{-2}) ^a
4U 1820–30	1021	2001-07-21	9	2.79	-7.91	7.6 ^b	1050	$1.31_{-0.14}^{+0.20}$
	1022	2001-09-12	9					
GX 9+9	703	2000-08-22	21	8.51	+9.04	$2.2_{-0.6}^{+1.2}$
Ser X-1	700	2000-06-13	76	36.12	+4.84	9.5–12.7 ^c	800–1070	...
Cyg X-1	107	1999-10-19	9	71.33	+3.07	2.0 ^d	110	6.3 ± 1.4
	3407	2001-10-28	21					2.4 ± 0.3
	3724	2002-07-30	14					2.9 ± 0.3
Cyg X-2	1102	1999-09-23	29	87.33	-11.32	11.4–15.3 ^c	2240–3000	1.1 ± 0.2
4U 1636–53	105	1999-10-20	29	332.91	-4.82	3.7–4.9 ^c	310–410	$2.6_{-0.3}^{+1.0}$
	1939	2001-03-28	26					
GX 339–4	4420	2003-03-17	74	338.94	-4.33	>6 ^c	>450	...
4U 1735–44	704	2000-06-09	24	346.05	-6.99	8.0–10.8 ^c	970–1310	3.4 ± 1.2
GX 349+2	715	2000-03-27	9	349.10	+2.75
	3354	2002-04-09	26					

^aOxygen column density measurement from Juett et al. (2004).

^bKuulkers et al. (2003, and references therein).

^cJonker & Nelemans (2004, and references therein).

^dGierliński et al. (1999).

that the accuracy increases for higher ionization states. We have also calculated photoelectric absorption cross-sections for Ne II and Ne III using the same method as for neutral neon (Gorczyca & McLaughlin 2005). We list the predicted positions of the Ne II, Ne III, and Ne IX lines from both sources in Table 1. Comparing the predicted wavelengths for the Ne II $1s-2p$ transition, we find that the two calculations differ by ≈ 25 mÅ, on the order of the error given by Behar & Netzer (2002). The oscillator strengths are consistent within a few percent. We note that the published natural width for Ne II in Behar & Netzer (2002) is incorrect and that the correct value is $2.710 \times 10^{14} \text{ s}^{-1}$ (Behar 2005, priv. comm.).

Using the full cross-sections for the neon species, we have checked that the neutral neon edge does not overlap with transitions from Ne II and Ne III. The Ne II resonance series limit is at ≈ 13.7 Å while the Ne III limit is at ≈ 13.3 Å. No resonance lines from Ne II or Ne III are coincident with the neutral neon edge. The edges are easily distinguishable given the spectral resolution of *Chandra*.

3. OBSERVATIONS AND SPECTRAL FITTING PROCEDURE

Our study was based on archival observations of nine bright X-ray binaries obtained with *Chandra* using the High Energy Transmission Grating Spectrometer (HETGS) in combination with the Advanced CCD Imaging Spectrometer (ACIS; Canizares et al. 2005). The HETGS spectra are imaged by ACIS, an array of six CCD detectors. The HETGS/ACIS combination provides both an undispersed (zeroth order) image and dispersed spectra from the gratings. The various orders are sorted using the intrinsic energy resolution of the ACIS CCDs. The HETGS carries two types of transmission gratings: the Medium Energy Gratings (MEGs) with a range of 2.5–31 Å (0.4–5.0 keV) and the High Energy Gratings (HEGs) with a range of 1.2–15 Å (0.8–10.0 keV). The first-order MEG (HEG) spectrum has a spectral resolution of $\Delta\lambda = 0.023$ Å (0.012 Å). The absolute wavelength accuracy of the MEG (HEG) is ± 0.011 Å

(0.006 Å).

In Table 2, we list the observations used in this analysis. The data sets were reduced using the standard CIAO threads⁵. In some cases, the zeroth-order data was not telemetered. For these observations, we estimated the zeroth-order position by finding the intersection of the grating arms and readout streak. After spectral extraction, the accuracy of the estimated zeroth-order position was verified by comparing the wavelengths of strong instrumental edges in both plus and minus sides of the spectra. Events collected during thermonuclear X-ray bursts were excluded from this analysis. Since the individual observations of 4U 1820–30 and 4U 1636–53 were brief, the spectra from multiple observations were combined for each source in order to improve statistics. Detector response files (ARFs and RMFs) were created for the +1 and -1 MEG and HEG spectra. The ARFs include the standard correction for the time-dependent change in the response due to a contaminant on ACIS. We then added the +1 and -1 orders to produce a combined MEG and HEG spectra from each source. Background spectra were also extracted. The MEG data were used for both the iron and neon edge fits, while the HEG data were used for the neon edge when reasonable signal-to-noise was found. All fitting was performed in count space. In this paper, we present the flux-corrected spectra in order that the reader may better visualize the interstellar features. These flux spectra are created in ISIS using the tool `flux_corr` which yields model-independent flux spectra.

3.1. Iron Edge Fit

We fit only the 16–18.5 Å wavelength range and binned the data to ensure at least 10 counts per bin. An absorbed power-law continuum model was used for all sources. We allowed the power-law model parameters to vary during the fits. The `tbvarabs` absorption model (Wilms et al. 2000) was used with the iron abundance set to zero to allow for an explicit modeling of the iron absorption. The equivalent hydrogen column

⁵ <http://asc.harvard.edu/ciao/threads/>

TABLE 3. FE EDGE PARAMETERS

Source	λ (Å)	N_{Fe} (10^{16} cm $^{-2}$)
4U 1820–30	17.505 ± 0.017	5.1 ± 1.9
GX 9+9	17.512 ± 0.015	7 ± 2
Ser X-1	17.502 ± 0.010	15 ± 3
Cyg X-1 ObsID 107	17.495 ± 0.009	$14.7^{+2.5}_{-1.9}$
Cyg X-1 ObsID 3407	17.501 ± 0.007	$10.6^{+0.7}_{-1.1}$
Cyg X-1 ObsID 3724	17.491 ± 0.004	9.6 ± 0.9
Cyg X-2	17.510 ± 0.012	5.6 ± 1.4
4U 1636–53	17.495 ± 0.010	10 ± 2
GX 339–4	17.505 ± 0.007	$14.4^{+2.2}_{-1.8}$
4U 1735–44	17.51 ± 0.02	6 ± 3
GX 349+2 ObsID 715	17.52 ± 0.04	69^{+11}_{-39}
GX 349+2 ObsID 3354	17.49 ± 0.02	26^{+17}_{-9}

density (N_{H}) of the `tbvarabs` model was set to equal a multiplicative factor times the iron column density (N_{Fe}), where the multiplicative factor was the inverse of the iron ISM abundance of Wilms et al. (2000). We modeled the iron absorption edge by using a custom multiplicative model based on the iron cross-section of Kortright & Kim (2000). The model parameters were N_{Fe} and the edge wavelength, defined as the position of the maximum cross-section of L_3 edge. Both were allowed to vary in the fits. The best-fit N_{Fe} and edge wavelengths are given in Table 3. All error estimates are 90%-confidence levels, unless otherwise noted, and do not include instrumental errors. Figures 2 and 3 show the data and best-fit model for each spectrum.

3.2. Neon Edge Fit

We fit only the 13.1–15.4 Å wavelength range and again binned the data to ensure at least 10 counts per bin. The continuum modeling used the same procedure as for iron (see § 3.1). We modeled the neutral neon absorption edge by using a custom multiplicative model based on the neon cross-section of Gorczyca (2000). The model parameters were N_{Ne} and the edge wavelength, defined as the position of the $1s$ - $3p$ resonance. Both were allowed to vary in the fits. Also included were three Gaussian absorption lines to measure the absorption by Ne II, Ne III, and Ne IX. Initial fits fixed the position of these lines to those found for GX 339–4 (Miller et al. 2004a) and the widths (sigma) to 0.005 Å (the instrument resolution). The earlier GX 339–4 result represents the best position identification for the low-ionization lines and was therefore used as the reference. Our results confirm the position of these lines. For sources where all three absorption lines were significantly detected, as opposed to only upper limits on their flux, we then refit the data, allowing the line positions and widths to vary. The best-fit parameters were used to determine the equivalent widths (EWs) of the lines. The best-fit N_{Ne} and edge wavelengths are given in Table 4, while the best-fit line positions, widths, and EWs are given in Table 5. Figures 4 and 5 show the data and best-fit model for each spectrum.

4. RESULTS AND ANALYSIS

We now compare the results of our analysis for the sample of sources. From this we will determine the line and edge positions, the relative abundances of the neutral

TABLE 4. NE EDGE PARAMETERS

Source	λ (Å)	N_{Ne} (10^{17} cm $^{-2}$)
4U 1820–30	14.294 ± 0.012	3.3 ± 1.2
GX 9+9	$14.304^{+0.008}_{-0.013}$	3.9 ± 1.3
Ser X-1	14.293 ± 0.007	$7.67^{+0.19}_{-0.7}$
Cyg X-1 ObsID 107	14.317 ± 0.007	7.1 ± 1.0
Cyg X-1 ObsID 3407	14.293 ± 0.004	$7.4^{+0.7}_{-0.3}$
Cyg X-1 ObsID 3724	14.256 ± 0.012	8.6 ± 0.7
Cyg X-2	14.294 ± 0.010	$2.3^{+0.9}_{-0.3}$
4U 1636–53	14.291 ± 0.012	4.9 ± 1.1
GX 339–4	14.281 ± 0.012	6.08 ± 0.13
4U 1735–44	14.315 ± 0.013	$2.2^{+1.3}_{-0.8}$
GX 349+2 ObsID 715	$14.30^{+0.05}_{-0.03}$	$14.40^{+0.11}_{-0.8}$
GX 349+2 ObsID 3354	$14.284^{+0.030}_{-0.013}$	13 ± 3

TABLE 5. NE LINE PARAMETERS

Source	λ (Å)	σ (Å)	EW (mÅ)
4U 1820–30	14.5065 (fixed)	0.005 (fixed)	> -5
	14.6067 (fixed)	0.005 (fixed)	> -7
	13.4420 (fixed)	0.005 (fixed)	$-4.8^{+1.9}_{-2.9}$
GX 9+9	14.511 ± 0.013	0.013 ± 0.010	-9^{+4}_{-7}
	14.610 ± 0.010	< 0.009	-5 ± 3
	13.438 ± 0.008	< 0.010	-6^{+2}_{-3}
Ser X-1	14.510 ± 0.004	< 0.014	$-7.2^{+2}_{-1.7}$
	14.606 ± 0.006	0.012 ± 0.006	-12 ± 3
	13.446 ± 0.002	< 0.007	-7.7 ± 1.4
Cyg X-1 ObsID 107	14.5065 (fixed)	0.005 (fixed)	> -6
	14.6067 (fixed)	0.005 (fixed)	-7 ± 3
	13.4420 (fixed)	0.005 (fixed)	> -3.6
Cyg X-1 ObsID 3407	14.511 ± 0.005	< 0.013	-4 ± 2
	14.612 ± 0.004	0.009 ± 0.006	-6 ± 3
	13.4420 (fixed)	0.005 (fixed)	> -2
Cyg X-1 ObsID 3724	14.5065 (fixed)	0.005 (fixed)	-3.0 ± 1.9
	14.6067 (fixed)	0.005 (fixed)	-3.2 ± 1.9
	13.4420 (fixed)	0.005 (fixed)	-5.3 ± 1.8
Cyg X-2	14.5065 (fixed)	0.005 (fixed)	> -3.5
	14.6067 (fixed)	0.005 (fixed)	-6.2 ± 2.7
	13.4420 (fixed)	0.005 (fixed)	> -5
4U 1636–53	14.502 ± 0.008	0.013 ± 0.010	-7 ± 4
	14.601 ± 0.012	< 0.04	-10 ± 7
	13.442 ± 0.006	< 0.015	-5 ± 2
GX 339–4	14.506 ± 0.003	0.008 ± 0.003	-9.4 ± 1.3
	14.607 ± 0.003	0.011 ± 0.003	-12 ± 2
	13.4425 ± 0.0019	0.005 ± 0.002	-11.6 ± 1.3
4U 1735–44	14.5065 (fixed)	0.005 (fixed)	> -6
	14.6067 (fixed)	0.005 (fixed)	> -12
	13.4420 (fixed)	0.005 (fixed)	-7^{+2}_{-4}
GX 349+2 ObsID 715	14.5065 (fixed)	0.005 (fixed)	> -13
	14.6067 (fixed)	0.005 (fixed)	> -37
	13.4420 (fixed)	0.005 (fixed)	> -20
GX 349+2 ObsID 3354	14.5065 (fixed)	0.005 (fixed)	> -21
	14.6067 (fixed)	0.005 (fixed)	> -27
	13.4420 (fixed)	0.005 (fixed)	> -18

and ionized species, and depletion fractions.

Our data are well fit by the metallic iron cross-section of Kortright & Kim (2000), although requiring a small shift in the position of the L_3 edge. This is comparable to previous studies of the iron edge (e.g., Lee et al. 2001; Schulz et al. 2002). The weighted mean position of the Fe- L_3 edge (taken as the position of maximum optical depth) is 17.498 ± 0.003 Å (errors are 90% confidence and do not account for the absolute instrumental wavelength accuracy of ± 0.011 Å; see Figure 6). Even including the absolute error, this value is significantly

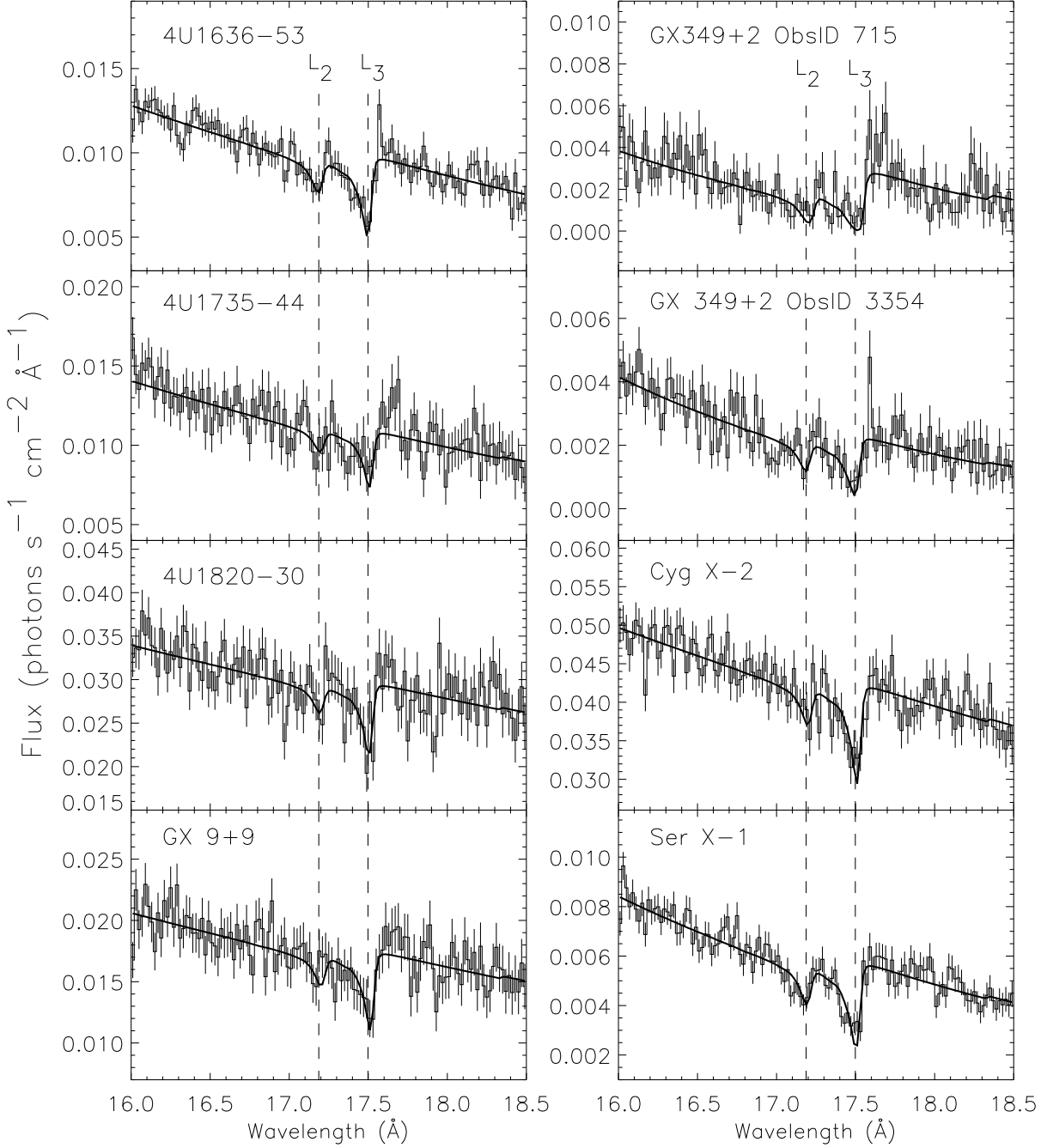


FIG. 2.— Flux spectra of the iron L -shell absorption region for the seven neutron star LMXBs included in this study. The data have been binned by a factor of two for illustrative purposes. The dashed lines indicate the positions of the L_2 and L_3 edges.

different from the measured positions of both the ferrous and ferric edges and lies between the two values (van Aken & Liebscher 2002). This may suggest that the ISM contains a combination of ferrous and ferric forms of iron. But we caution that the energy resolution of the laboratory data (0.8 eV=20 mÅ at 17.5 Å; van Aken & Liebscher 2002) is large enough to make either value consistent with our measurement. The spacing of the L_2 and L_3 edges is well fit by our model and is more consistent with ferrous iron. This would imply that

the laboratory measurement of the wavelength of ferrous iron is off by ≈ 19 mÅ.

If both ferrous and ferric forms are present in the ISM, we would expect a double-peaked structure in the combined edge. We searched the residuals from the best-fit for our data. A negative residual at 17.40 Å was found, although with low significance, $< 3\sigma$. Even if true, the wavelength of the feature is too small to be attributable to a contribution from ferric iron, which we would expect at 17.45 Å if our best-fit position is from ferrous iron. In

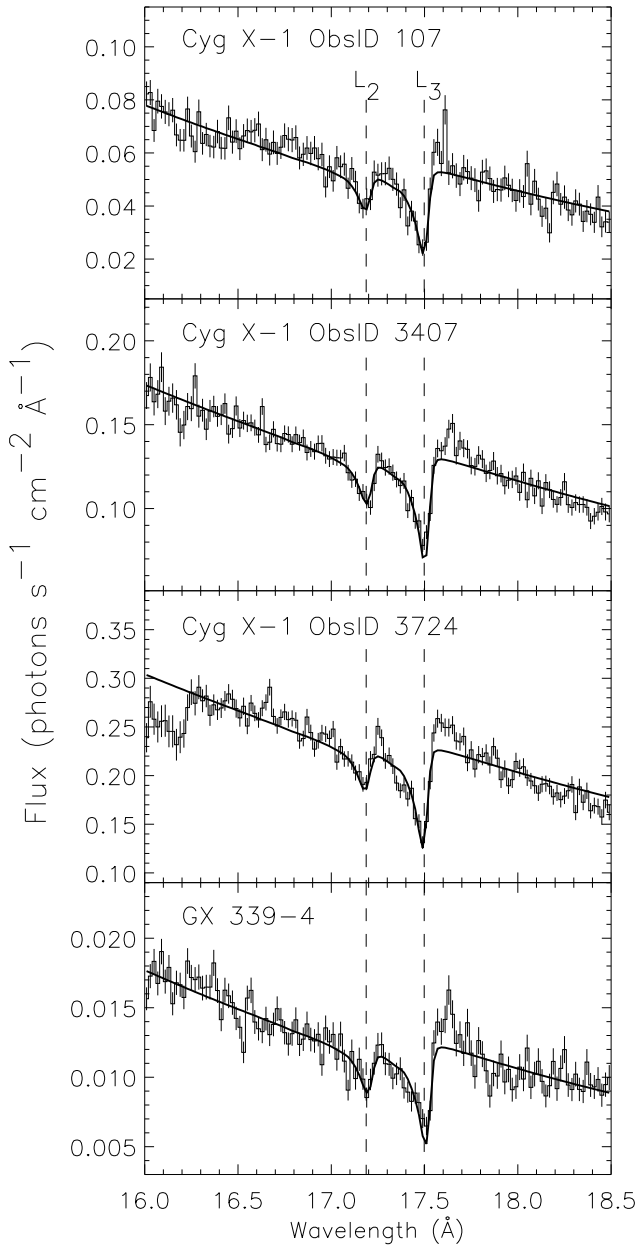


FIG. 3.— Flux spectra of the iron L -shell absorption region for the two black hole X-ray binaries included in this study. The data have been binned by a factor of two for illustrative purposes. The dashed lines indicate the positions of the L_2 and L_3 edges.

addition, a check of the effective area versus wavelength for the sources with the most prominent residuals found sharp variations in the effective area, a signature of hot pixels or columns, in the iron wavelength range. We also note the positive residuals just high of the edge position (17.6 Å). We know of no atomic or molecular features that would produce such a residual. It is also possible that these residuals are due to hot pixels or columns.

For the neutral neon edge, we find a weighted mean position of the $1s-3p$ transition of 14.295 ± 0.003 Å (see Figure 7). This is consistent with laboratory measurements (e.g., Coreno et al. 1999). We note that the the-

oretical position of Gorczyca (2000) was calibrated to this laboratory measurement. For the ionized neon lines, we find a weighted mean position of 14.608 ± 0.002 Å for Ne II, 14.508 ± 0.002 Å for Ne III, and 13.4439 ± 0.0013 Å for Ne IX. The Ne IX position is consistent with theoretical and observational measurements, accounting for the absolute instrument error. The Ne II and Ne III lines, however, are ≈ 20 mÅ off of the theoretical predictions. This is within the quoted errors for the theoretical calculations (Behar & Netzer 2002). In this case, the error is more significant for the theory than the observations. We encountered a similar effect when identifying the neutral and low-ionization lines from oxygen (Paper I). We note that our best-fit positions for the Ne II and Ne III lines are consistent with the results of Miller et al. (2004a).

4.1. Relative Abundances of Oxygen, Iron, and Neon

Using the column density measurements, including the oxygen column density measurements of Paper I, we can now directly measure the abundance ratios in the X-ray domain. This measurement is a function not only of the interstellar abundances, but also of the depletion of the elements into dust grains. We have chosen to use neon as the calibration point for these measurements, thereby providing O/Ne and Fe/Ne ratios, for two reasons. First, as a noble gas, neon should not be depleted. Second, as the lowest wavelength edge of the set presented here, it lies near the middle of the *Chandra* wavelength band. Observations of higher column density sources will show edges from neon, magnesium, and silicon. Therefore, abundance ratios relative to neon will allow us to directly compare the ISM abundances of various elements, e.g., oxygen and silicon, which could not be done with a single source in the X-ray waveband.

We calculated the abundance ratios (by number) for the entire sample and for the neutron star (NS) LMXBs only. While the black hole systems in our sample are known to show intrinsic features (Schulz et al. 2002; Feng et al. 2003; Miller et al. 2003; Miller et al. 2004a), the NS LMXBs show no emission or absorption features that are intrinsic to the system. NS LMXBs which do show intrinsic features are not included in this study. We therefore take the NS subsample to be indicative of the ISM properties and show the black hole systems relative to this subsample. We note that the inclusion of the black hole systems in this study may seem unnecessary given their intrinsic features, but they provide the highest signal-to-noise spectra allowing us to make more accurate measurements of the line and edge positions.

In Figure 9, we compare the neon and oxygen column densities for our sample. For all the systems, we find a O/Ne ratio of 3.7 ± 0.3 . When we restrict our sample to the NS systems, we find O/Ne = 5.4 ± 1.6 . The difference in the measurements is driven by the low oxygen column measurements for two of the Cyg X-1 datasets. We note that while the oxygen column for Cyg X-1 shows a factor of 2 difference between the three datasets, the neon column density measurements are all consistent within errors. This is likely due to material local to the source (see Paper I and references therein).

Our abundance ratio measurement for the NS systems is consistent with O/Ne = 5.6 obtained from the ISM abundances of Wilms et al. (2000). This is also consistent with standard solar abundance ratios (O/Ne = 6.6;

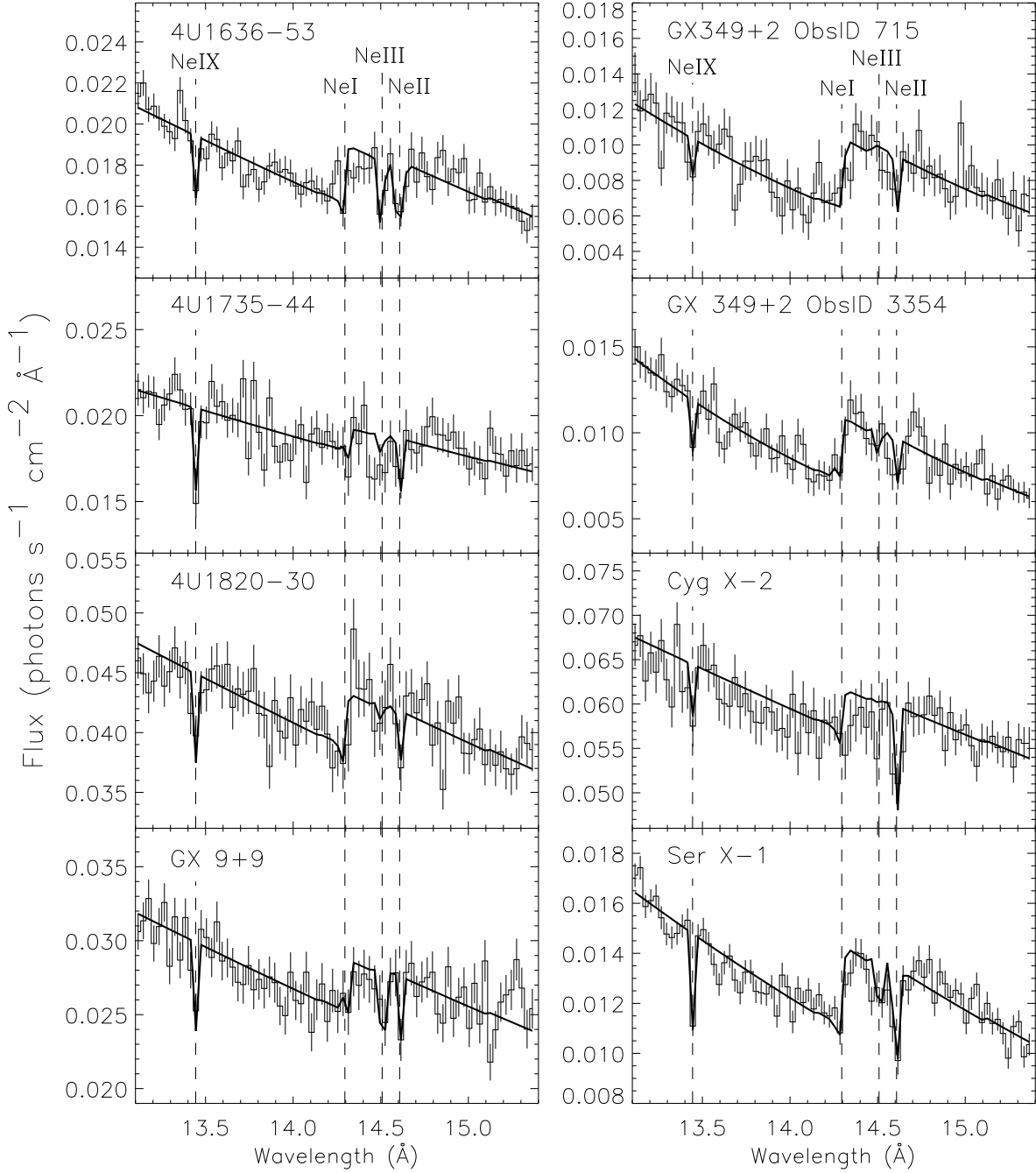


FIG. 4.— Flux spectra of the neon K -shell absorption region for the seven neutron star LMXBs included in this study. The data have been binned by a factor of three for illustrative purposes. The dashed lines indicate the positions of the identified features.

e.g., Lodders 2003; Asplund et al. 2005b). Interestingly, our results exclude the abundance ratio of Drake & Testa (2005), $O/Ne=2.4$. One possible explanation is that our two studies cover a very different extent in the Galaxy. All of our sources are $\gtrsim 2$ kpc from the Sun, while the Drake & Testa (2005) sample of stars are all within 100 pc.

Our best-fit O/Ne ratio also allows for roughly 45% of the oxygen in the ISM to be located in grains (see derivation below and Appendix A), although we note

that the large error on the O/Ne ratio allows no real constraint. More precise measurements of the O/Ne ratio are needed to probe the depletion in the ISM.

The Fe/Ne ratio, however, shows a large deviation from the Wilms et al. (2000) ISM abundance ratio of 0.309 (see Figure 10). Including all systems, we find $Fe/Ne=0.159\pm 0.013$, while for NS systems only, $Fe/Ne=0.20\pm 0.03$. Both measurements are significantly different than the ISM value. The sense of the discrepancy is that we are finding less iron in the ISM than we

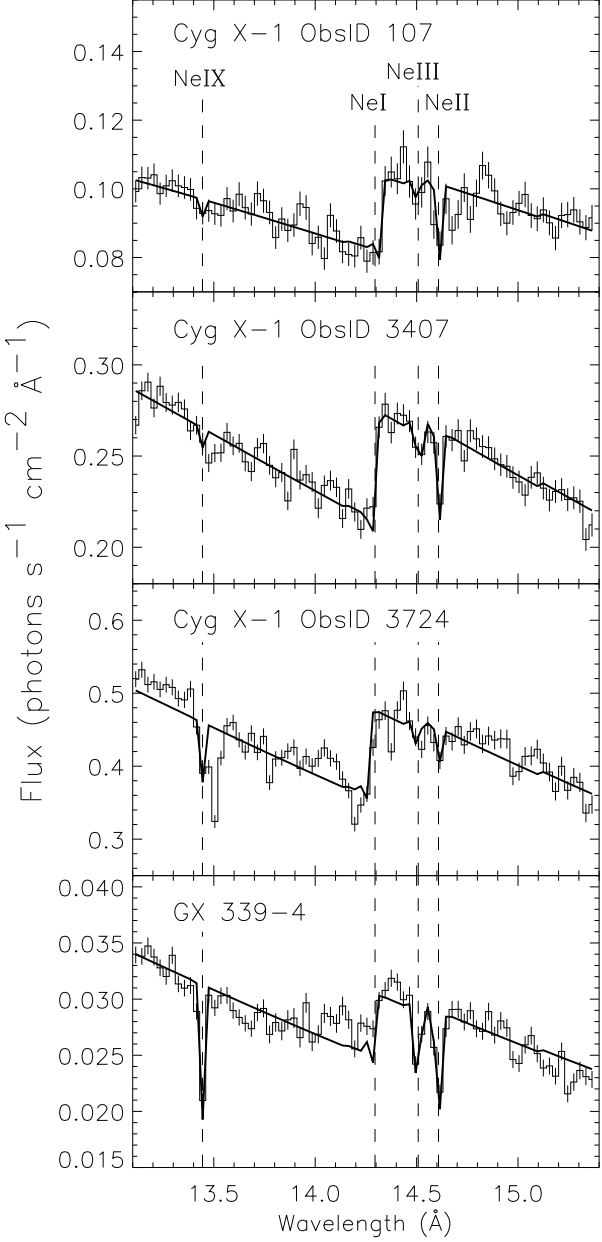


FIG. 5.— Flux spectra of the neon K -shell absorption region for the two black hole X-ray binaries included in this study. The data have been binned by a factor of three for illustrative purposes. The dashed lines indicate the positions of the identified features.

would expect. The discrepancy between the measured and predicted Fe/Ne abundance ratio is likely the result of depletion in the ISM. As mentioned previously, atoms in dust grains have a lower effective cross-section than the same atoms in gas. Therefore, using the gas cross-section (as we have) would cause the column density measurements to be lower than the true value.

Attributing the abundance ratio difference to depletion, we can estimate the amount of iron located in dust grains. The total optical depth of iron, τ_{Fe} , is the sum of the contributions from gas and dust grains. The gaseous iron optical depth is the gas phase cross-section times

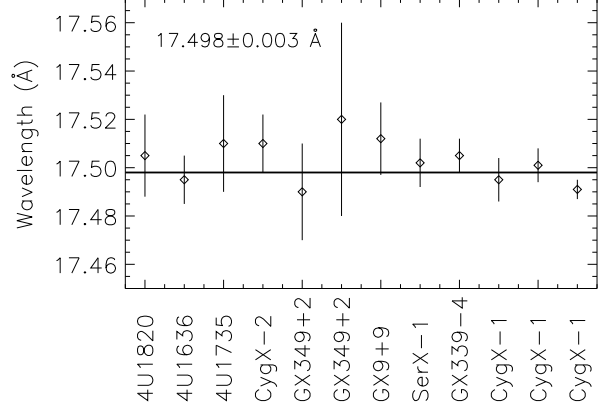


FIG. 6.— Best fit position of the iron L_3 absorption edge, defined as the position of maximum cross-section. The weighted mean value of the line position is given. All quoted errors are statistical only and do not include the instrumental wavelength error of ± 0.011 Å (FWHM).

the column density of iron in the gas phase, given by $\sigma_{\text{gas}} N_{\text{Fe,gas}}$. The optical depth from iron in dust is the grain cross-section times the column density of iron in grains given by $\sigma_{\text{grain}} N_{\text{Fe,grain}}$. The depletion factor, β , measures the amount of the total iron column density found in grains, $N_{\text{Fe,grain}} = \beta N_{\text{Fe}}$. Similarly, the gas column density is $N_{\text{Fe,gas}} = (1 - \beta) N_{\text{Fe}}$. Finally, the dust cross-section can be related to the gas cross-section by a factor, f , as shown in Appendix A. Combining this we find

$$\tau_{\text{Fe}} = \sigma_{\text{gas}} (1 - \beta) N_{\text{Fe}} + f \sigma_{\text{gas}} \beta N_{\text{Fe}} = \sigma_{\text{gas}} N_{\text{Fe}} (1 - \beta + f\beta). \quad (1)$$

Our analysis assumes that $\tau_{\text{Fe}} = \sigma_{\text{gas}} N_{\text{Fe}}$. Therefore we can relate our measured iron column density, $N_{\text{Fe,meas}}$, to the true column density by $N_{\text{Fe,meas}} = N_{\text{Fe}} (1 - \beta + f\beta)$. Since we do not know the true N_{Fe} , we must use abundances ratios to measure depletion. Using abundance relative to neon allows us to avoid additional depletion effects that would be present with oxygen. The relationship between the measured Fe/Ne abundance ratio and the ISM ratio is given by

$$(\text{Fe/Ne})_{\text{meas}} = (1 - \beta + f\beta) \times (\text{Fe/Ne})_{\text{ISM}}, \quad (2)$$

assuming $\beta = 0$ for neon. Given our measured Fe/Ne ratio, the ISM abundance ratio from Wilms et al. (2000), and the value of f calculated in Appendix A, we find that $\beta = 2.9 \pm 0.8$, which is unphysical since β is constrained to the range 0–1.

Obviously, one or more of our assumptions is invalid. It is possible that the ISM abundances of either iron or neon is incorrect. Wilms et al. (2000) claim errors for the ISM abundances of 0.1 dex or higher. A neon abundance 0.1 dex larger is enough to account for the discrepancy and constrain $\beta > 0.5$. A slightly greater neon abundance is not at present problematic for our measured O/Ne ratio, given the large error bars. Similarly, a lower iron abundance could also account for the difference.

We have also tested the possibility that the dust grain cross-section could be miscalculated. Assuming the Wilms et al. (2000) abundances, for various depletion factors, $\beta = 0.7$ –0.95, we find that Equation 2 gives

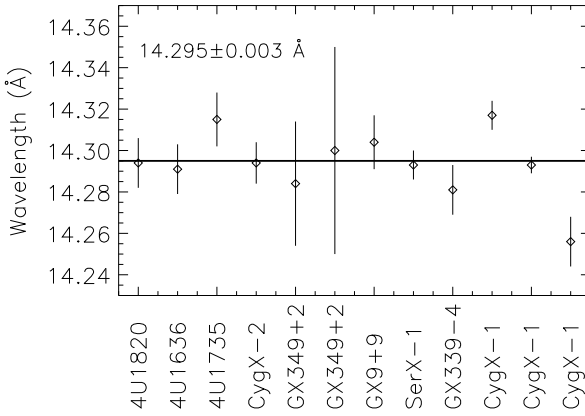


FIG. 7.— Best fit position of the 1s-3p transition from Ne I. The weighted mean value of the line position is given. All quoted errors are statistical only and do not include the instrumental wavelength error of ± 0.011 Å (FWHM).

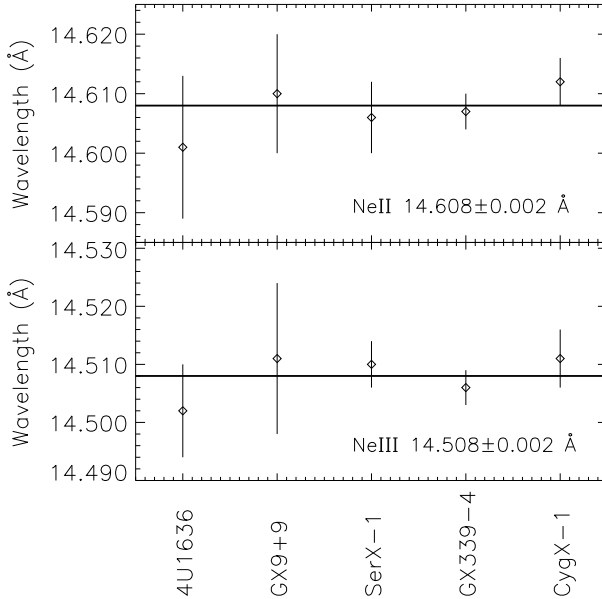


FIG. 8.— Best fit positions of the 1s-2p transitions from Ne II (top panel) and Ne III (bottom panel). All quoted errors are statistical only and do not include the instrumental wavelength error of ± 0.011 Å (FWHM).

values of $f=0.4\text{--}0.7$, significantly lower than our calculated value. We have calculated f , as shown in Appendix A, for various assumptions, including the dust model (Mathis et al. 1977; Weingartner & Draine 2001), abundances, variations in depletion factors of the astrophysically abundant elements, grain mass density, and the gas cross-section for iron. Most of these parameters do not make a large difference to the value of f .

Only the cross-section and grain mass density are able to make a significant effect, although they must be more than 5 times larger to bring the measured and predicted results into agreement. A difference this large in the iron cross-section is unlikely. First, we are already using the maximum value of the cross-section,

not the average value over the edge which would give a lower cross-section. In addition, the cross-section of Kortright & Kim (2000) compares well with lower-resolution measurements at wavelengths away from the high-resolution structure. Therefore the cross-section difference between the L_3 maximum and the lower wavelength absorption would have to be substantially greater than found by Kortright & Kim (2000). Since our data fit both the high-resolution structure and the lower wavelength absorption, we would expect to see deviations in our data from the chosen model if this was the case. Such deviations are not found and we therefore conclude that the iron edge model is accurate in its structure and scale to at least 10%.

Finally, we address a final assumption in the calculation of f , which is a homogeneous distribution of the elements in grains. Spitzer & Fitzpatrick (1993) suggested that interstellar silicate grains may have a iron-rich core with a magnesium-mantle. Such a scenario would provide more shielding to the iron atoms, producing a lower value of f .

4.2. Ionized Neon Abundances

The diffuse ISM has four major phases: cold neutral, warm neutral, warm ionized, and hot ionized (Heiles & Kulkarni 1987). The strength of the ionized neon lines can be used to constrain the properties of these phases. The Ne II and Ne III lines are most likely associated with the warm ionized medium (WIM), while the neutral edges will be primarily from the warm neutral medium (WNM). From an ultraviolet observation of the Galactic halo star HD 93521, Spitzer & Fitzpatrick (1993) found that the WIM coincided with the WNM. Other studies (Howk & Savage 1999; Reynolds et al. 1995) have found similar results. This allows us to make a direct comparison of the column densities from the neutral and low ionization neon lines from which the ionization of the ISM can be measured.

The ionized abundances can be estimated from a curve of growth analysis (see Paper I). We used the theoretical cross-section of Gorczyca (2005; in prep.) to calculate the curve of growth for Ne II and Ne III assuming thermal velocities of 20, 100, and 200 km s $^{-1}$. Using the oscillator strengths and natural widths of Behar & Netzer (2002) gives consistent results. In Figure 11, we plot the EW in the ionized lines versus the neutral neon column density for each source. Given an ionized abundance, $A = N_X/N_{\text{NeI}}$, one can then overlay the curves of growth calculated from the theoretical line properties. The best-fit abundance is determined by comparing the theoretical curves at different values of A to the data points. We note that there is a degeneracy between the thermal velocity and the ionized abundance. Given the low significance of our EW measurements, we only estimate the ionized abundances. We find that Ne II/Ne I ≈ 0.3 and Ne III/Ne I ≈ 0.07 .

Our analysis attributes the ionized neon lines to interstellar material. In our oxygen edge study, we argued that an interstellar interpretation is correct, since the EWs of the lines correlated better with the neutral column density than with the source luminosity (see Paper I). The same trend is suggested by the ionized neon lines, although at much less significance. Obviously, more ac-

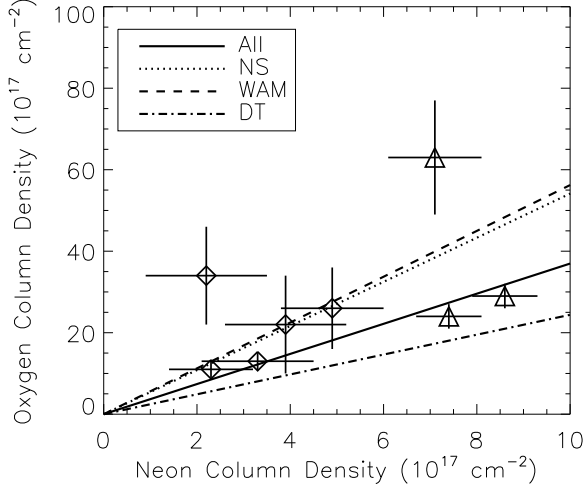


FIG. 9.— Comparison of the neutral oxygen and neon column densities for our sample of sources. The best fit O/Ne ratio is plotted for all sources (solid line) and the neutron star LMXBs only (dotted line). We have overplotted the ISM O/Ne ratio of Wilms et al. (2000, dashed line) and the stellar coronal measurement of Drake & Testa (2005, dashed-dotted line). The best fit value for the NS LMXBs is in good agreement with the ISM value. None of our values are consistent with the Drake & Testa (2005) O/Ne ratio.

curate measurements are required to verify this trend.

It is interesting to note that the EWs of the low-ionization neon lines from GX 339–4 give a result in line with the NS LMXB trend. This suggests that the low and neutral absorption along the line of sight to GX 339–4 is consistent with an interstellar origin. On the other hand, the EWs for the low-ionization neon lines from Cyg X-1 do not follow the same trend. In the oxygen study, Cyg X-1 showed large variations in the column densities of the neutral and ionized lines (Paper I). We attributed those changes to circumstellar material in the binary. The variations in the neon features are less substantial, which may imply something interesting about the source of the ionizing flux.

The Ne IX absorption should originate in the hot phase of the ISM. With a higher temperature and lower density, the hot phase will have a larger scale height than the warm phases which contain the neutral and low ionization lines. Therefore, a direct comparison is not appropriate. Instead, we follow Yao & Wang (2005) and compare the Ne IX column densities as a function of z , the distance from the Galactic plane (see Figure 12). We overplot their best-fit disk distribution. The Ne IX column densities were calculated from a curve of growth assuming a gas temperature of 2.4×10^6 K (Yao & Wang 2005). Our results compare reasonably well with their best-fit model, which is not surprising given the large overlap of sources. Again, we see variations in the Cyg X-1 (open triangles) column densities. The data point that deviates the most from the model is from GX 339–4 (filled triangle). This confirms that a sizable contribution to the Ne IX line is due to a local contribution, which is reasonable given the detection of other hydrogenic and helium-like lines in the spectrum of this source (Miller et al. 2004a).

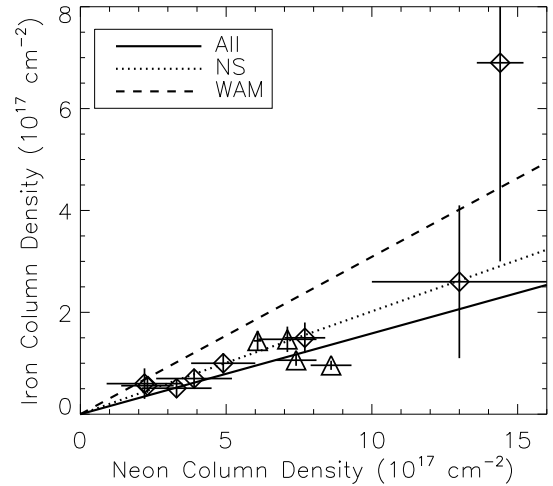


FIG. 10.— Comparison of the neutral iron and neon column densities for our sample of sources. The best fit Fe/Ne ratio is plotted for all sources (solid line) and the neutron star LMXBs only (dotted line). We have overplotted the ISM Fe/Ne ratio of Wilms et al. (2000, dashed line). Our best fit Fe/Ne ratio is significantly lower than the ISM value. We attribute this to depletion of iron into dust grains in the ISM.

5. DISCUSSION

We have presented a global study of the neon K -shell and iron L -shell absorption in the ISM. Combined with our previous study of oxygen absorption (Paper I), we have determined the neutral abundances ratios between oxygen, iron, and neon. We find $O/Ne = 5.4 \pm 1.6$, in line with current ISM abundances. Our Fe/Ne abundance of 0.20 ± 0.03 is lower than the expected ISM value of 0.309 , suggesting that iron is depleted in the ISM. We note that unless depletion is taken into account in X-ray absorption models, a subsolar iron abundance may be found. This subsolar iron abundance can be due only to the ISM and does not *a priori* signify an astrophysically interesting result related to the source properties.

We also detected absorption lines from Ne II, Ne III, and Ne IX in a number of the sources. We attribute these lines to the ISM. A curve of growth analysis found that the large-scale ionization of neon in the ISM is $Ne\,II/Ne\,I \approx 0.3$ and $Ne\,III/Ne\,I \approx 0.07$. The implied column densities in the Ne IX lines are consistent with the model of Yao & Wang (2005) for all sources except the black hole LMXB GX 339–4.

5.1. Ionization of the Warm ISM

The ISM of the Galaxy is typically modeled as a multiphase medium (see e.g., McKee & Ostriker 1977). The phases have different temperatures, densities, and ionizations. The following discussion focuses on two of the phases, the warm neutral and warm ionized mediums (WNM and WIM, respectively). These two phases have similar temperatures ($T \sim 10^4$ K) but different hydrogen ionization fractions. In the WNM, the ionized hydrogen fraction $H\,II/H_{total} \sim 0.1$, while in the WIM, $H\,II/H_{total} \gtrsim 0.8$ (see Howk et al. 2003, and references therein).

Our implied ionization fractions for Ne II and Ne III

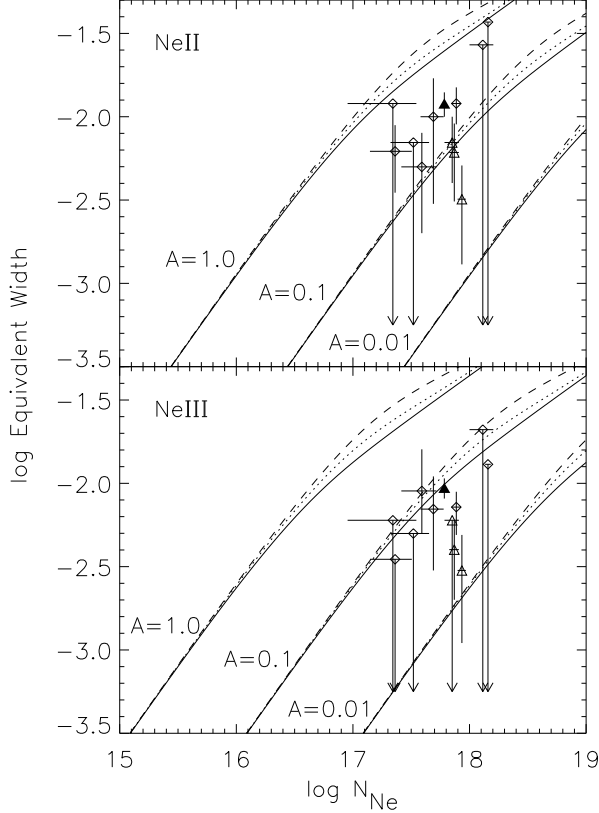


FIG. 11.— Curve of growth for the Ne II and Ne III absorption features. Plotted are the measured values of the neutral neon column density, N_{Ne} , and the EW in the ionized neon absorption lines. The diamonds mark the NS LMXB systems, the open triangle marks the black hole binary Cyg X-1, and the filled triangle marks the black hole LMXB GX 339-4. Overlayed are the theoretical predictions for the relationship between the column density and EW in the lines. The solid, dotted, and dashed lines indicate the predicted EWs for velocity dispersion of 20, 100, and 200 km s^{-1} , respectively. Also included are predicted EWs for various abundances ($A = N_{\text{X}}/N_{\text{NeI}}$) relative to neutral neon. From these figures, we can estimate the relative abundances for Ne II and Ne III relative to Ne I.

are greater than we found for oxygen, $\text{O II}/\text{O I} \approx 0.1$ and $\text{O III}/\text{O I} \approx 0.05$ (Paper I). With higher first ionization potentials, we would expect the ionization of neon to track that of helium in the ISM. Measurements of the $\text{He I } \lambda 5876/\text{H}\alpha$ line intensity ratio suggest a helium ionization fraction $n(\text{He II})/n(\text{He}_{\text{total}}) \lesssim 0.27$ in regions where the hydrogen is primarily ionized (i.e. in the WIM; Reynolds & Tufte 1995). This has been taken to imply that the helium is primarily neutral in the WIM, since the alternative explanation, that helium is primarily fully ionized, appears inconsistent with the low ionization of other elements, particularly sulfur and nitrogen.

Our measured neon ionization ratios include the contributions from all phases of the ISM. In the following, we attribute the neutral and low-ionization features to the WNM and WIM only. These phases should be the dominant contributors. We would like to estimate the $\text{Ne II}/\text{Ne}_{\text{tot}}$ ratio in the WIM to compare with the helium result. To do this, we assume that the Ne II and Ne III lines are produced in the WIM only, while the

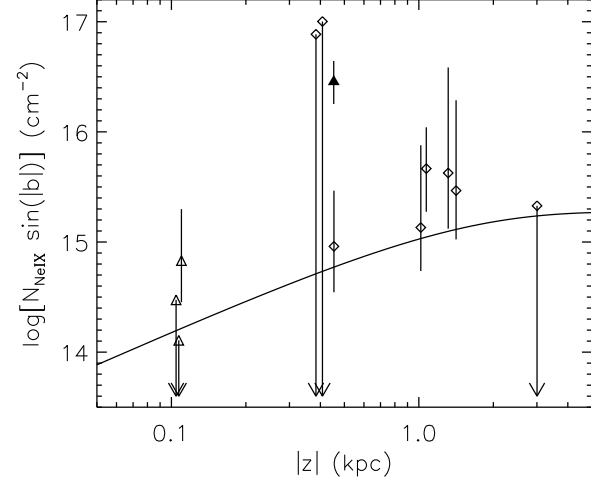


FIG. 12.— Ne IX column density as a function of source distance above the plane. Column densities were calculated from the EWs assuming a gas temperature of 2.4×10^6 K. For systems with no known distance, we assume a distance of 8.5 kpc, while for GX 339-4 we used the lower limit on the distance of 6 kpc. Slight shifts in $|z|$ were applied for illustrative purposes. Overplotted is the best fit disk distribution of Yao & Wang (2005). The diamonds mark the NS LMXB systems, the open triangle marks the black hole binary Cyg X-1, and the filled triangle marks the black hole LMXB GX 339-4. Notice that the data for GX 339-4 is the most discrepant from the model, confirming a local contribution to the Ne IX line.

neutral neon absorption includes contributions from both the WNM and WIM. Given the higher ionization potential of neon compared to hydrogen, we believe this is valid based on the hydrogen ionization in each phase. We must make two other assumptions: first, the Ne I, Ne II, and Ne III are the dominant contributors to the total interstellar neon budget, and second, that a significant fraction ($\gtrsim 75\%$) of the neutral neon is found in the WNM, as opposed to the WIM. Combining these assumptions, we find

$$\left(\frac{\text{Ne II}}{\text{Ne}_{\text{tot}}} \right)_{\text{WIM}} = \frac{(\text{Ne II}/\text{Ne I})_{\text{tot}}}{\text{Ne I}_{\text{WIM}}/\text{Ne I}_{\text{tot}} + (\text{Ne II}/\text{Ne I})_{\text{tot}} + (\text{Ne III}/\text{Ne I})_{\text{tot}}}. \quad (3)$$

This work directly measures $(\text{Ne II}/\text{Ne I})_{\text{tot}}$ and $(\text{Ne III}/\text{Ne I})_{\text{tot}}$, and we are assuming $\text{Ne I}_{\text{WIM}}/\text{Ne I}_{\text{tot}} \lesssim 0.25$.

Our results then yield $\text{Ne II}/\text{Ne}_{\text{tot}} \gtrsim 0.4$ in the WIM. This is different from the helium results, although we note that the exact values of the ionization fraction of Ne II and Ne III are dependent on the assumed thermal velocity of the ISM, which may make the difference between the measured ionizations of helium and neon less significant. In addition, our measurement of the Ne III/Ne I ratio seems incompatible with standard OB star models for the ionization of the WIM (see e.g., Sembach et al. 2000). Extra heating has been studied to explain the properties of optical emission and absorption lines (e.g., Slavin et al. 2000; Elwert & Dettmar 2005), but these results concentrate on the elements of interest

in the optical. Therefore, neon ionization fractions are not given. One possible explanation for our neon ionization results is that the lines of sight probed by the X-ray studies contain a larger WIM fraction relative to the WNM.

X-ray studies probe different lines of sight than traditional optical and ultraviolet work. Many of our sight lines are towards the center of the Galaxy and the Galactic bulge. Optical and ultraviolet studies concentrate on the Perseus arm of the Galaxy which is roughly anti-Galactic center ($120^\circ < l < 150^\circ$). While X-ray allows us to probe larger distances and cover a greater extent of the Galaxy, this also makes it difficult to reconcile X-ray results with other ISM studies. Future work will use multiwavelength studies of X-ray binaries to compare X-ray ISM results with optical and ultraviolet studies.

5.2. The Warm Absorber in GX 339–4

Miller et al. (2004a) identified the Ne II, Ne III, and Ne IX lines in the spectrum of GX 339–4 and attributed them to an AGN-like warm absorber. Our results show that the Ne IX line shows a clear excess column density over the expected interstellar component. The measured Ne IX column density for GX 339–4 is $\approx 3.9 \times 10^{17} \text{ cm}^{-2}$. For Galactic latitude of GX 339–4 and a distance of 6 kpc, the ISM model predicts a column density of $7.8 \times 10^{15} \text{ cm}^{-2}$. While the exact distance to GX 339–4 is unknown, the model column density as a function of Galactic scale height reaches a maximum value of $2.5 \times 10^{16} \text{ cm}^{-2}$. From these values, we estimate that only $\approx 2\text{--}6\%$ of the measured Ne IX column density to GX 339–4 is due to the hot ISM. This seems reasonable given the detection of other highly ionized lines in the spectrum of the source.

The properties of the Ne II and Ne III lines how-

ever, are completely consistent with the other LMXBs in our sample. The measured line widths are all $\approx 20 \text{ m}\text{\AA}$ off from the theoretical calculations of Behar & Netzer (2002), within the quoted errors for the calculations. Similar wavelength shifts were also required in our study of the oxygen edge (Paper I). The line widths are also consistent with the other sources in our sample, and are more likely indicative of the resolution of the instrument rather than an astrophysical origin. Finally, the implied ionized abundances of Ne II and Ne III from the GX 339–4 data are consistent with the NS LMXBs. If these lines had a local component, we should see deviations from these relationships. We note that variations in the EW of these lines were claimed by Miller et al. (2004b) but we caution that comparisons between *Chandra*/HETG and *XMM*/RGS spectra are suspect for narrow absorption features due to the factor of two difference in the spectral resolution between the instruments. Narrow features easily detectable by *Chandra* can be substantially washed out by the RGS resolution. We therefore claim that the low-ionization neon features in GX 339–4 are completely consistent with an interstellar origin.

We thank E. Behar for providing us with his data and for useful discussions on the relevant atomic physics. Support for this work was provided by the National Aeronautics and Space Administration through the Smithsonian Astrophysical Observatory contract SV3-73016 to MIT for Support of the Chandra X-Ray Center, which is operated by the Smithsonian Astrophysical Observatory for and on behalf of the National Aeronautics Space Administration under contract NAS8-03060. TWG was supported in part by NASA APRA grant NNG0-4GB58G and by NASA SHP SR&T grant NNG05GD41G.

REFERENCES

Anders, E., & Grevesse, N. 1989, *Geochim. Cosmochim. Acta*, 53, 197

Asplund, M., Grevesse, N., Guedel, M., & Sauval, A. J. 2005a, *Nature*, submitted as Brief Communications, (astro-ph/0510377)

Asplund, M., Grevesse, N., & Sauval, A. J. 2005b, in ASP Conf. Ser. 336: Cosmic Abundances as Records of Stellar Evolution and Nucleosynthesis, 25–38

Bahcall, J. N., Basu, S., & Serenelli, A. M. 2005, *ApJ*, 631, 1281

Behar, E., & Netzer, H. 2002, *ApJ*, 570, 165

Brinkman, A. C., Mewe, R., Langerwerf, T., Heise, J., & Peacock, A. 1985, *Space Science Reviews*, 40, 201

Canizares, C. R., et al. 2005, *PASP*, 117, 1144

Chantler, C. T. 1995, *Journal of Physical and Chemical Reference Data*, 24, 71

Coreno, M., Avaldi, L., Camilloni, R., Prince, K. C., de Simone, M., Karvonen, J., Colle, R., & Simonucci, S. 1999, *Phys. Rev. A*, 59, 2494

de Vries, C. P., den Herder, J. W., Kaastra, J. S., Paerels, F. B., den Boggende, A. J., & Rasmussen, A. P. 2003, *A&A*, 404, 959

Draine, B. T. 2003, *ARA&A*, 41, 241

Drake, J. J., & Testa, P. 2005, *Nature*, 436, 525

Elwert, T., & Dettmar, R.-J. 2005, *ApJ*, 632, 277

Feng, Y. X., Tennant, A. F., & Zhang, S. N. 2003, *ApJ*, 597, 1017

Futamoto, K., Mitsuda, K., Takei, Y., Fujimoto, R., & Yamasaki, N. Y. 2004, *ApJ*, 605, 793

Gierliński, M., Zdziarski, A. A., Poutanen, J., Coppi, P. S., Ebisawa, K., & Johnson, W. N. 1999, *MNRAS*, 309, 496

Gorczyca, T. W. 2000, *Phys. Rev. A*, 61, 024702

Gorczyca, T. W. & McLaughlin, B. M. 2005, *Bull. Am. Phys. Soc.*, 50, 39

Heiles, C., & Kulkarni, S. R. 1987, in *NATO ASIC Proc. 210: Physical Processes in Interstellar Clouds*, 13–33

Henke, B. L., Gullikson, E. M., & Davis, J. C. 1993, *Atomic Data and Nuclear Data Tables*, 54, 181

Howk, J. C., & Savage, B. D. 1999, *ApJ*, 517, 746

Howk, J. C., Sembach, K. R., & Savage, B. D. 2003, *ApJ*, 586, 249

Jonker, P. G., & Nelemans, G. 2004, *MNRAS*, 354, 355

Juett, A. M., & Chakrabarty, D. 2003, *ApJ*, 599, 498

Juett, A. M., Psaltis, D., & Chakrabarty, D. 2001, *ApJ*, 560, L59

Juett, A. M., Schulz, N. S., & Chakrabarty, D. 2004, *ApJ*, 612, 308 (Paper I)

Kahn, S. M., Seward, F. D., & Chlebowski, T. 1984, *ApJ*, 283, 286

Kortright, J. B., & Kim, S. 2000, *Phys. Rev. B*, 62, 12216

Kuulkers, E., den Hartog, P. R., 't Zand, J. J. M., Verbunt, F. W. M., Harris, W. E., & Cocchi, M. 2003, *A&A*, 399, 663

Lee, J. C., Ogle, P. M., Canizares, C. R., Marshall, H. L., Schulz, N. S., Morales, R., Fabian, A. C., & Iwasawa, K. 2001, *ApJ*, 554, L13

Lee, J. C., Reynolds, C. S., Remillard, R., Schulz, N. S., Blackman, E. G., & Fabian, A. C. 2002, *ApJ*, 567, 1102

Lodders, K. 2003, *ApJ*, 591, 1220

Martin, P. G. 1970, *MNRAS*, 149, 221

Mathis, J. S., Rumpl, W., & Nordsieck, K. H. 1977, *ApJ*, 217, 425

McKee, C. F., & Ostriker, J. P. 1977, *ApJ*, 218, 148

Miller, J. M., et al. 2004a, *ApJ*, 601, 450

Miller, J. M., Raymond, J., Fabian, A. C., Wijnands, R., van der Klis, M., & Lewin, W. H. G. 2004b, *The Astronomer's Telegram*, 221, 1

Miller, J. M., Wojdowski, P., Schulz, N. S., Marshall, H. L., Fabian, A. C., Remillard, R. A., Wijnands, R., & Lewin, W. H. G. 2005, 620, 398

Nicastro, F., et al. 2003, *Nature*, 421, 719

Paerels, F., et al. 2001, *ApJ*, 546, 338

Reynolds, R. J., & Tufte, S. L. 1995, *ApJ*, 439, L17

Reynolds, R. J., Tufte, S. L., Kung, D. T., McCullough, P. R., & Heiles, C. 1995, *ApJ*, 448, 715

Savage, B. D., & Sembach, K. R. 1996, *ARA&A*, 34, 279

Schattenburg, M. L., & Canizares, C. R. 1986, *ApJ*, 301, 759

Schmelz, J. T., Nasraoui, K., Roames, J. K., Lippner, L. A., & Garst, J. W. 2005, *ApJ*, 634, L197

Schulz, N. S., Cui, W., Canizares, C. R., Marshall, H. L., Lee, J. C., Miller, J. M., & Lewin, W. H. G. 2002, *ApJ*, 565, 1141

Sembach, K. R., Howk, J. C., Ryans, R. S. I., & Keenan, F. P. 2000, *ApJ*, 528, 310

Sembach, K. R., et al. 2003, *ApJS*, 146, 165

Slavin, J. D., McKee, C. F., & Hollenbach, D. J. 2000, *ApJ*, 541, 218

Spitzer, L. J., & Fitzpatrick, E. L. 1993, *ApJ*, 409, 299

Takei, Y., Fujimoto, R., Mitsuda, K., & Onaka, T. 2002, *ApJ*, 581, 307

Ueda, Y., Mitsuda, K., Murakami, H., & Matsushita, K. 2005, *ApJ*, 620, 274

van Aken, P. A., & Liebscher, B. 2002, *Physics and Chemistry of Minerals*, 29, 188

Verner, D. A., Yakovlev, D. G., Band, I. M., & Trzhaskovskaya, M. B. 1993, *Atomic Data and Nuclear Data Tables*, 55, 233

Weingartner, J. C., & Draine, B. T. 2001, *ApJ*, 548, 296

Weisskopf, M. C., O'Dell, S. L., Paerels, F., Elsner, R. F., Becker, W., Tennant, A. F., & Swartz, D. A. 2004, *ApJ*, 601, 1050

Wilms, J., Allen, A., & McCray, R. 2000, *ApJ*, 542, 914

Woo, J. W. 1995, *ApJ*, 447, L129

Yao, Y., & Wang, Q. D. 2005, *ApJ*, 624, 751

APPENDIX

DERIVATION OF CROSS-SECTION FOR DUST GRAINS

The derivation of the cross-section for dust grains presented in Wilms et al. (2000) includes the contribution of all elements. For our data, we need the iron dust cross-section only. Therefore, we present a rederivation of the calculation of the dust cross-section for a single element, Z .

We begin by considering Equation A7 of Wilms et al. (2000):

$$\tau_{\text{grains}} = N_{\text{H}} \xi_{\text{g}} \int_0^{\infty} \frac{dn_{\text{gr}}(a)}{da} \sigma_{\text{geom}} [1 - \exp(-\langle \sigma \rangle \langle N \rangle)] da , \quad (\text{A1})$$

where N_{H} is the hydrogen column density, ξ_{g} is the number of grains per hydrogen atom, $dn_{\text{gr}}(a)/da$ is the grain size distribution assuming spherical grains of size a , $\sigma_{\text{geom}} = \pi a^2$ for spherical grains, $\langle \sigma \rangle$ is the average photoelectric absorption cross-section of the grain material and $\langle N \rangle$ is the column density in a grain.

For our purposes, we want τ_{grains} of element Z . N_{H} can be directly related to the element column density N_Z by $N_{\text{H}} = N_Z / A_Z$, where A_Z is the ISM abundance of element Z . Since we are considering a single element, $\langle \sigma \rangle$ is just the gas phase cross-section of that element, σ_{gas} .

To calculate $\langle N \rangle$ for a single element, we follow Wilms et al. (2000), and assume that the grains have a homogeneous chemical composition and are spherical with size a . We consider only the contribution of element Z to $\langle N \rangle$, remembering that element Z makes up only part of the total mass of the grains. We find

$$\langle N \rangle = \frac{4\rho_Z a}{3\mu_Z} , \quad (\text{A2})$$

where ρ_Z is the mass density of element Z in interstellar grains and μ_Z is the atomic mass. The mass density ρ_Z is related to the total grain mass density ρ by

$$\rho_Z = \rho \times A_Z \beta_Z \mu_Z / \sum_Z A_Z \beta_Z \mu_Z , \quad (\text{A3})$$

where β_Z is the depletion fraction of element Z . The calculation of ρ_Z takes into account the contribution of all other elements to the total dust content of the ISM.

For a single element, the number of grains per atom ξ_{g} is given by

$$\xi_{\text{g}} = A_Z \beta_Z \mu_Z / \int \frac{dn_{\text{gr}}(a)}{da} \times \rho_Z \times \frac{4}{3} \pi a^3 \times da . \quad (\text{A4})$$

Substituting the above relationships into Equation A1, we find

$$\tau_{\text{grains}} = N_Z \beta_Z \mu_Z \int_0^{\infty} \frac{dn_{\text{gr}}(a)}{da} \pi a^2 [1 - \exp(-\sigma_{\text{gas}} \frac{4\rho_Z a}{3\mu_Z})] da / \int \frac{dn_{\text{gr}}(a)}{da} \rho_Z \frac{4}{3} \pi a^3 da . \quad (\text{A5})$$

For our analysis, we are interested in the determining the value of f , the factor which relates the dust cross-section to the gas-phase cross-section, $\sigma_{\text{grain}} = f \sigma_{\text{gas}}$.

The grain optical depth $\tau_{\text{grain}} = \sigma_{\text{grain}} N_{Z,\text{grain}}$ where $N_{Z,\text{grain}}$ is the column density of element Z found in grains. The grain column density is given by the total column density times the depletion factor, β_Z , i.e. $N_{Z,\text{grain}} = \beta_Z N_Z$. Therefore, we can substitute for the grain optical depth, $\tau_{\text{grains}} = f \sigma_{\text{gas}} \beta_Z N_Z$. Solving for f , we find

$$f = \frac{3\mu_Z}{4\rho_Z \sigma_{\text{gas}}} \int_0^{\infty} \frac{dn_{\text{gr}}(a)}{da} a^2 [1 - \exp(-\frac{4\rho_Z \sigma_{\text{gas}}}{3\mu_Z} a)] da / \int \frac{dn_{\text{gr}}(a)}{da} \times a^3 \times da , \quad (\text{A6})$$

after some simplification.

We can now use the above equation to calculate f under various assumptions. Our initial assumptions use the ISM abundances and depletion factors given by Wilms et al. (2000). We take $\rho = 1 \text{ g cm}^{-3}$ and $dn_{\text{gr}}(a)/da$ from Mathis et al. (1977). We note that σ_{gas} is a function of energy.

For iron, we assume a single value for σ_{gas} , which is the maximum value of the cross-section at the L_3 edge. Using the maximum value of σ_{gas} gives the lowest value of f . We find $f = 0.88$ for iron.

Similarly, for oxygen we can calculate the value of f . The dominant K -shell edge for oxygen occurs at the $1s-np$ series limit for the $S = 3/2$ final state (see Paper I). Using the cross-section value at this limit to find the value of f yields $f = 0.90$.